Int. J. Electrochem. Sci., 16 **(2021)** Article ID: 210848, doi: 10.20964/2021.08.40

International Journal of
ELECTROCHEMICAL
SCIENCE
www.electrochemsci.org

Short Communication

Hydrothermal synthesis of Ag–ZnO nanostructures as an advanced material for photoelectrochemical applications

Nusayba A. Albadarin[1,*], *Mohd Sobri Takriff*[1], *Mohd Nur Ikhmal Salehmin*[2], Wong Wai Yin[2], *Sin Tee Tan*[3], *Abdul Amir H. Kadhum*[1], Lorna Jeffery Minggu[2], *Aymen Alamarneh*[4], *Eman Shqirat*[4]

[1] Department Chemical and Process Engineering, Faculty of Engineering and Built Environment, Universiti Kebangsaan Malaysia, 43600 UKM Bangi, Selangor, Malaysia
[2] Fuel Cell Institute, Universiti Kebangsaan Malaysia, 43600 UKM Bangi, Selangor, Malaysia
[3] Department of Physics, Faculty of Science, Universiti Putra Malaysia, 43400 UPM Serdang, Selangor, Malaysia
[4] Chemistry Department, Faculty of Science and Technology, Al-Quds University, P.O. Box 89, Palestine
[*]E-mail: albadarin.nusayba@gmail.com

Received: 1 May 2021 / *Accepted:* 15 June 2021 / *Published:* 30 June 2021

Ag–ZnO nanostructures with a controllable morphology and optical band structure were prepared via a hydrothermal process. The relationship among crystallite size, morphology and optical bandgap of the synthesised Ag–ZnO nanostructures in Ag molar ratio functions was elucidated. A comparative photoelectrochemical (PEC) analysis was performed using two types of photoanodes, namely, ZnO and Ag–ZnO. After Ag loading, the thickness of ZnO nanorods decreased to 13.7 nm, indicating that the growth of ZnO nanorods was disrupted by the presence of Ag. Accordingly, the optical bandgap of the sample revealed that it underwent bathochromic change. PEC testing was performed in 0.5 M Na_2SO_4 electrolyte under 100 mW cm^{-2} xenon light irradiation. Results showed that the 0:1 Zn:Ag sample generated a photocurrent density that was tenfold higher than that of pristine ZnO photoanode. The enhancement in photocurrent density might be attributed to the low optical energy bandgap that facilitated the charge transport process. This study presented a facile method for fabricating Ag–ZnO photoanodes with an excellent photocurrent generation for robust PEC applications.

Keywords: Ag–ZnO, absorption spectra, microsphere, nanorod, photocurrent density

1. INTRODUCTION

The utilisation of zinc (II) oxide (ZnO) in photocatalysis applications has considerably expanded owing to its remarkable physical and chemical stability, high oxidative capacity and high electron mobility. Furthermore, ZnO is a widely available and nontoxic material that provides a large surface area in nanomaterials [1-4]. Although it is commonly used as an electron transport layer, ZnO has a low absorption efficiency for visible light because of its large bandgap. Therefore, the surface of ZnO nanostructures must be modified to enhance their light absorption and carrier generation abilities. To date, several experiments to alter the surface properties of ZnO nanostructures have been conducted via different physical and chemical approaches [4-6]. For instance, several studies incorporated quantum dots into or doped ZnO nanostructures with noble metals [7-9]. The modification of semiconductors by using different noble metals as dopants, especially in heterogeneous photocatalysis, has attracted increased attention [10, 11]. Nevertheless, surface modification is not limited to surface modification of materials for various applications but also can be extended as a functionalisation approach. The morphology of several noble metals, such as gold (Au) [12], platinum (Pt) [13] and silver (Ag) [14], has been extensively analysed owing to their excellent catalytic properties.

Among various noble metals that can be used as a dopant, Ag is considered the most promising candidate because of its good carrier transport properties. Moreover, Ag is highly stable with a small orbital energy and a large ionic size. Ag is reportedly a good charge collector in photovoltaic cells [10, 15]. Similarly, AgO and Ag_2O have a high degradation efficiency in organic pollutants under visible light illumination because of their nontoxic nature and narrow range of direct energy bandgap that ranges from 0.9 eV to 1.1 eV [16]. Ag nanoparticles (NPs) are considered excellent elements that can be utilised in the development of electronic devices in the future [17].

The dynamics of Ag in the photoactivity of metal oxide-based catalysts under visible light are being extensively investigated. Ag-modified ZnO reportedly exhibits enhanced photocatalytic activity because of the high carrier density on the catalyst’s surface that arise from point defects. According to the literature, the coexistence of metallic Ag in semiconductors results in excellent catalytic activity [18, 19]. Accordingly, the photocatalytic activity of ZnO/Ag semiconductors can be improved owing to their heterojunction structure. In the present study, the physicochemical and photoelectrochemical (PEC) properties of Ag incorporated as a dopant onto ZnO nanorods (NRs) at varying ratios were characterised and analysed. Notably, Ag–ZnO photoanodes were fabricated via a green and non-energy-intensive hydrothermal method.

2. MATERIALS AND METHODS

Ag–ZnO samples were prepared via a hydrothermal process by using different Ag molar ratios. Fluorine-doped tin oxide (FTO) substrates were separately sonicated in methanol and acetone for 10 min. Subsequently, the substrates were rinsed with deionised (DI) water and dried with nitrogen (N_2) gas. A ZnO thin film was deposited on the substrates via radio frequency (RF) magnetron sputtering (Kurt J. Lesker PVD-75). A Zn metal target with a purity of >99.99% (PO 1210097/KS, Aci Alloys Inc.) was used. During deposition, the sputter power was fixed at 150 W, and the deposition was conducted for 30 min at ambient temperature. During sputtering, oxygen (O_2) gas was purged into the system to produce translucent ZnO thin films. The film-coated FTO substrates were then subjected to heat treatment at 350 °C for 2 h in the air to produce a 200 nm-thick seed layer. A precursor solution for fabricating pristine ZnO NRs was prepared by dissolving 40 mM of zinc nitrate hexahydrate ($Zn(NO_3)_2.6H_2O$, Sigma-Aldrich) and hexamethylenetetramine (HMT) ($(CH_2)_6.N_4$, Sigma-Aldrich) in 100 mL of DI water. The solution was continuously stirred for 50 min at room temperature and then transferred to a Teflon-lined autoclave. The seed layer-coated FTO substrate was inserted in the sealed autoclave and heated at 95 °C for 5 h in a laboratory oven. Afterward, the obtained samples were rinsed with DI water several times and dried at 100 °C for 30 min. Finally, all samples were annealed in an N_2-purged tube furnace (OTF-1200X) at 500 °C for 2 h. The samples were fabricated with five different molar ratios of Zn to Ag, i.e., 1:0, 3:1, 1:1, 1:3 and 0:1. The precursor solution was prepared by dissolving zinc acetate ($Zn(CH_3COO)_2.2H_2O$, Sigma Aldrich), HMT ($(CH_2)_6{\cdot}N_4$, Sigma-Aldrich) and silver nitrate ($AgNO_3$, Sigma-Aldrich) in 100 mL DI water and stirred for 45 min. The same step for annealing pristine ZnO NRs was applied for Ag–ZnO samples.

2.1. Characterisation of ZnO NRs and Ag–ZnO nanostructures

The crystalline structures of the fabricated ZnO NRs and Ag–ZnO nanostructures were determined via X-ray diffraction (XRD, Brucker D8). The test was conducted under CuKα irradiation with a wavelength λ of 0.154 nm. The surface morphology of the samples was examined via field-emission scanning electron microscopy (FESEM, Zeiss Merlin Compact) at an accelerating voltage of 3 keV. The presence and distribution of elements on the surface of the samples were identified via electron-dispersive X-ray spectroscopy (EDX, Zeiss Merlin Compact). The optical transmission spectra of all samples were measured via UV–Vis–NIR spectroscopy with wavelengths ranging from 100 nm to 1,000 nm.

2.2. PEC activity measurements

The photoresponse of the samples was measured using a three-electrode system enclosed in a custom-made photocell. The nanostructured samples were used as a working electrode with an exposed area of 1 cm^2. A platinum wire and Ag/AgCl saturated in 3 M KCl were employed as a counter and a reference electrode, respectively. These electrodes were immersed in 0.5 M Na_2SO_4 electrolyte. The PEC activity of the samples was measured via linear scan voltammetry (Ametek VersaSTAT 4) with a scan rate of 0.05 Vs^{-1} under 100 mW cm^{-2} xenon light irradiation. Prior to testing, the electrolyte was purged with N_2 gas for 30 min.

3. RESULTS AND DISCUSSION

3.1. Characterisation of the physicochemical properties of Ag–ZnO nanostructures

The structural properties of the prepared samples and the presence of various compounds were investigated via XRD. The diffraction pattern of Ag–ZnO samples is given in Figure 1.

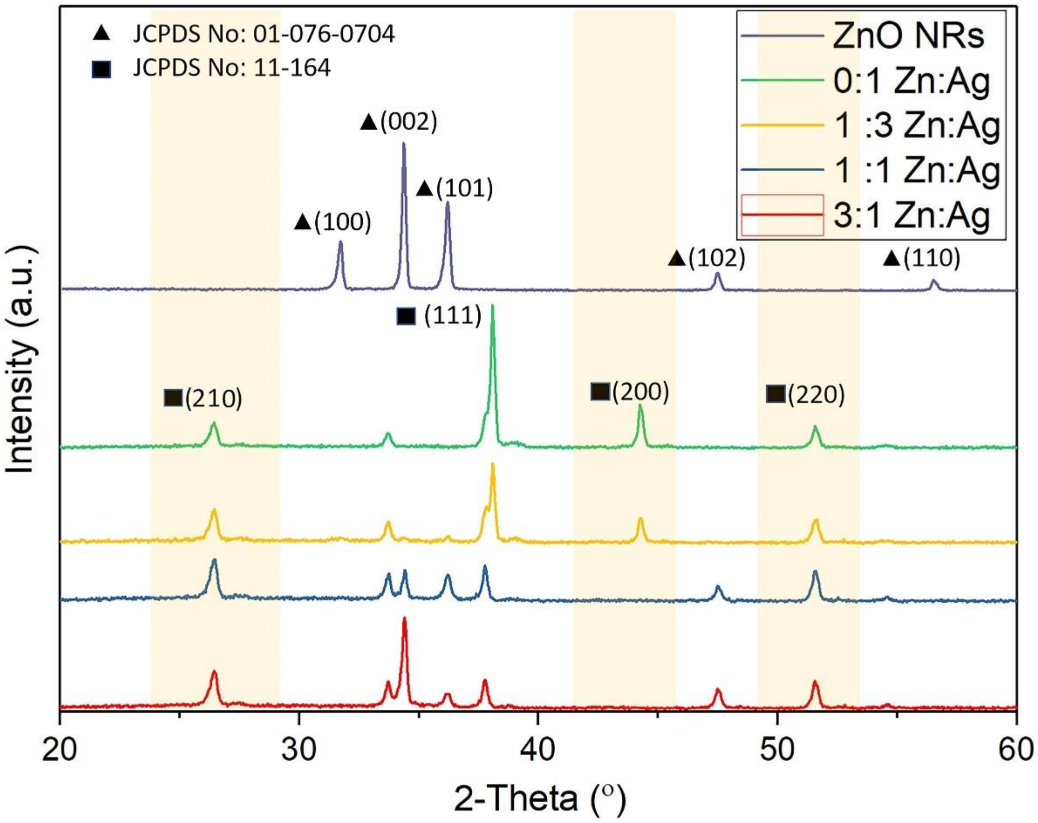

Figure 1. XRD diffraction spectra for ZnO nanorod and Zn: Ag sample.

The ZnO NRs seed layer sample had five diffraction patterns at $2\theta = 31.83°$, 34.49°, 36.34°, 47.63° and 56.69°, which were indexed to the (100), (002), (101), (102) and (110) planes, respectively, of ZnO hexagonal wurtzite (JCPDS Card No. 01-076-0704). Upon the growth of Ag-ZnO on the seed layer, the seed layer peaks have disappeared as the X-ray beam was not able to penetrate through the thick layer of Ag-ZnO to the seed layer. When Ag was growth onto the ZnO NR seed layer (0:1 Zn:Ag), four main diffraction patterns were detected at $2\theta = 26.3°$, 38°, 44.2° and 51.5°, which were indexed to the (210), (111), (200) and (220) planes, respectively, of cubic Ag_2O (JCPDs Card No.11-164). Two main observations were obtained when the Zn:Ag ratio increased from 3:1 to 0:1. Firstly, the characteristic peaks of cubic Ag_2O has increased in intensity, with the crystal phase of ZnO at 34.49°, 36.34° and 47.63° resemble the seed layer diffraction patterns gradually diminished. Secondly, there observed with a single peak in the 3:1 and 1:1 samples at approximately 37.5°; with further increase in the Ag composition in the alloy to 1:3 and 0:1, the co-existence of a new peak at 38° is observed. The presence of different peaks with the change in the alloy composition has indicated a crystal phase change has occurred, which is in good agreement with the FESEM results obtained in Figure 2 which shows the different morphology between the two aforementioned sets of samples. For the 3:1 and 1:1 samples, the nanorod structure is clearly observed due to the dominance of ZnO in the alloy; meanwhile, at lower ZnO composition at 1:3 and 0:1, the irregular microsphere structure of Ag as the dominant compound is vividly observed. This observation is a typical phenomenon of doping effect in ZnO which has been reported by many [20-23].

The average crystallite size (*D*) of the samples was calculated using the Debye–Scherrer equation as expressed in equation (1):

$$D = \frac{0.9\lambda}{\beta_{hkl}cos\theta}, \qquad (1)$$

where λ is the wavelength of incident X-ray beam (1.541° A), θ is Bragg's diffraction angle and β_{hkl} is the full width at half-maximum of the dominant peaks. When the molar ratio of Ag was increased, the crystalline size of the Ag–ZnO samples considerably decreased from 33.41 nm to 19.96 nm.

FESEM micrographs of the top and cross-sectional views of the ZnO NRs and Ag–ZnO nanostructures grown on the FTO substrate are provided in Figure 2. The samples with mole ratios of Zn:Ag = 1:0, 3:1 and 1:1 showed a high density of vertically aligned ZnO NRs coated with Ag NPs. When the molar ratio of Ag was increased, an irregular microsphere nanostructure grew on the FTO surface. The Ag NPs likely started to agglomerate on the surface. For the 1:3 Zn:Ag sample, a combination of ZnO NRs and microspheres was found on the surface. For the 0:1 Zn:Ag sample, an irregular microsphere was distributed on the FTO surface. The thickness of the samples was also analysed using Image J software. After Ag incorporation, the thickness of the NRs decreased from 29.73 nm to 13.7 nm. This observation could be attributed to the decrease in growth rate of the ZnO NRs induced by Ag NPs [24].

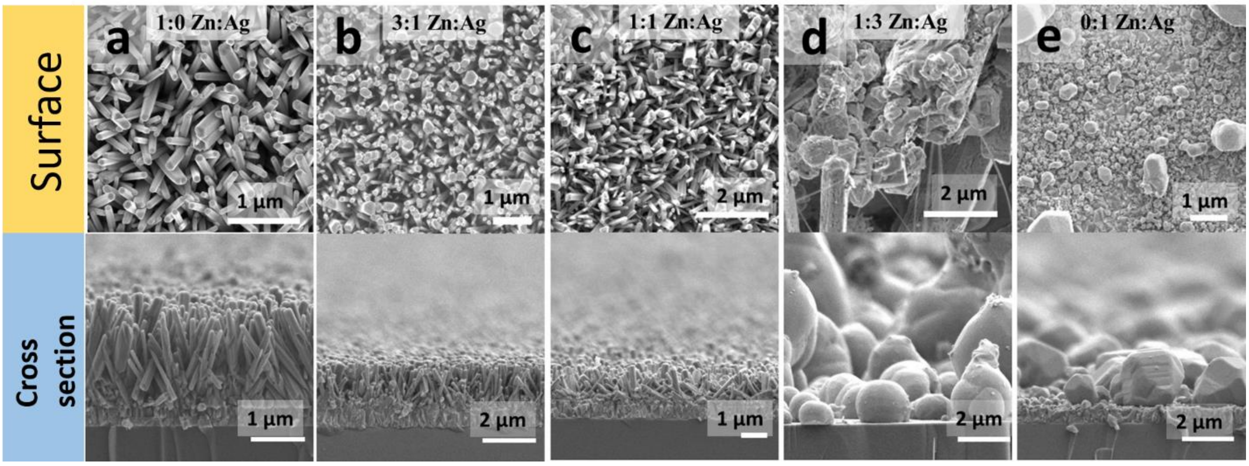

Figure 2. FESEM top view and cross sectional view of ZnO Nanorod and Ag-ZnO sample

The elements existing in the Ag–ZnO nanostructures were identified and measured via EDX. The EDX spectra are summarised in Figure 3. Three elements, namely, Ag, Zn and O, were detected in the samples, suggesting that the prepared samples were of high purity. The weight (%) of Ag increased from 11wt.% to 52.0wt.% with the concentration of Ag dopants compared with that of the 0:1 Zn:Ag sample (84.4wt.%). The detailed weights (%) of the samples are given in Table 1. Elemental distribution was determined via EDX mapping. The areas marked in yellow, red and green represent Zn, O and Ag, respectively. Zn, O and Ag were found to be evenly distributed on the surface of FTO. Zn was clearly the dominant element (Figures 3a and 3b); hence, the weight of Ag did not exceed 12%. However, Ag had the highest ratio (Figures 3c and 3d). The results confirmed that the microspheres basically formed from Ag, whereas the NRs originated from Zn and O elements. This result further confirmed that of XRD analysis.

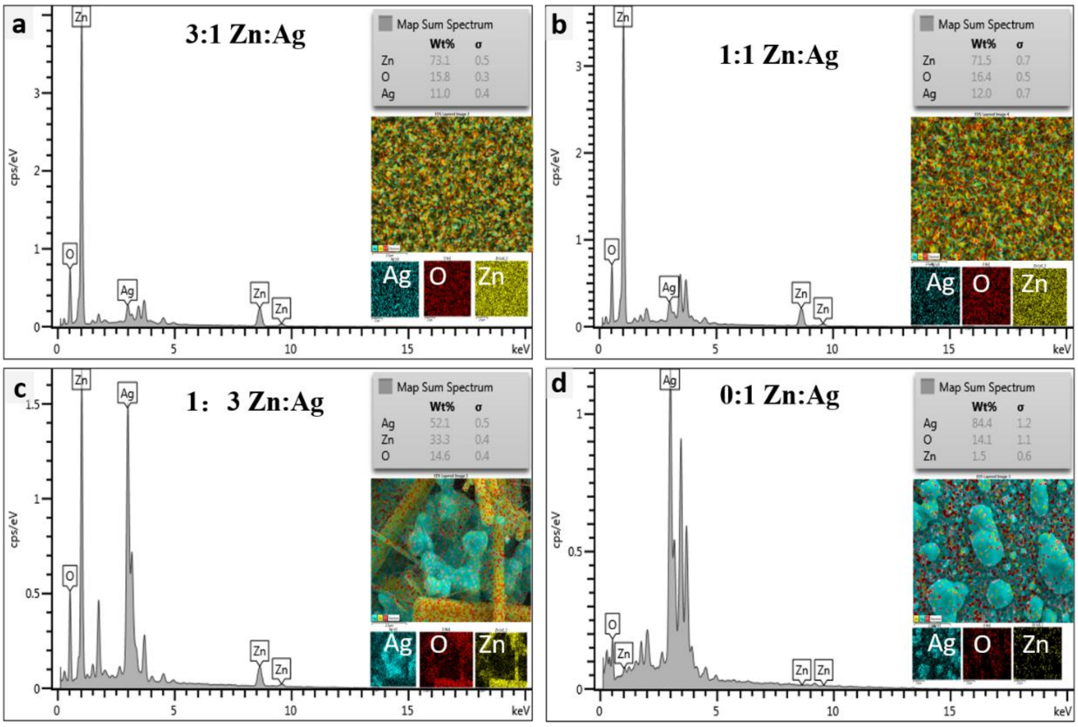

Figure 3. The EDX spectra for Ag-ZnO sample

Table 1. Elemental analysis of Ag–ZnO nanostructures prepared from different molar ratios of Zn:Ag.

Sample	Zn (wt.%)	Ag (wt.%)	O (wt.%)
Pure ZnO NRs	60.03	0	30.97
3:1 Zn:Ag mole ratio	73.1	11	15.8
1:1 Zn:Ag mole ratio	71.5	12	16.4
1:3 Zn:Ag mole ratio	33.3	52.1	14.6
0:1 Zn:Ag mole ratio	1.5	84.4	14.1

The absorption spectra of the ZnO NRs and Ag–ZnO nanostructures are plotted in Figure 4. Compared with that of the ZnO NRs, the absorption ability for visible light of the Ag–ZnO nanostructures was substantially enhanced. When the dopant ratio of Ag was increased, the absorption intensity of the Ag–ZnO nanostructures also increased because the density of the Ag NPs increased. Therefore, the enhancement in visible light absorption of the sample was likely due to the energy gap structures that formed in the Ag–ZnO electrode and promoted the transfer of electrons in the visible region. Furthermore, the band gap in the Ag–ZnO nanostructures was analysed using a Tauc relation. Notably, Ag had a high absorption ability toward visible light because of localised surface plasmon resonance. As seen in Figure 4, the band gap energy of Ag–ZnO decreased to 2.2 eV when the concentration of Ag increased (Zn:Ag = 0:1).

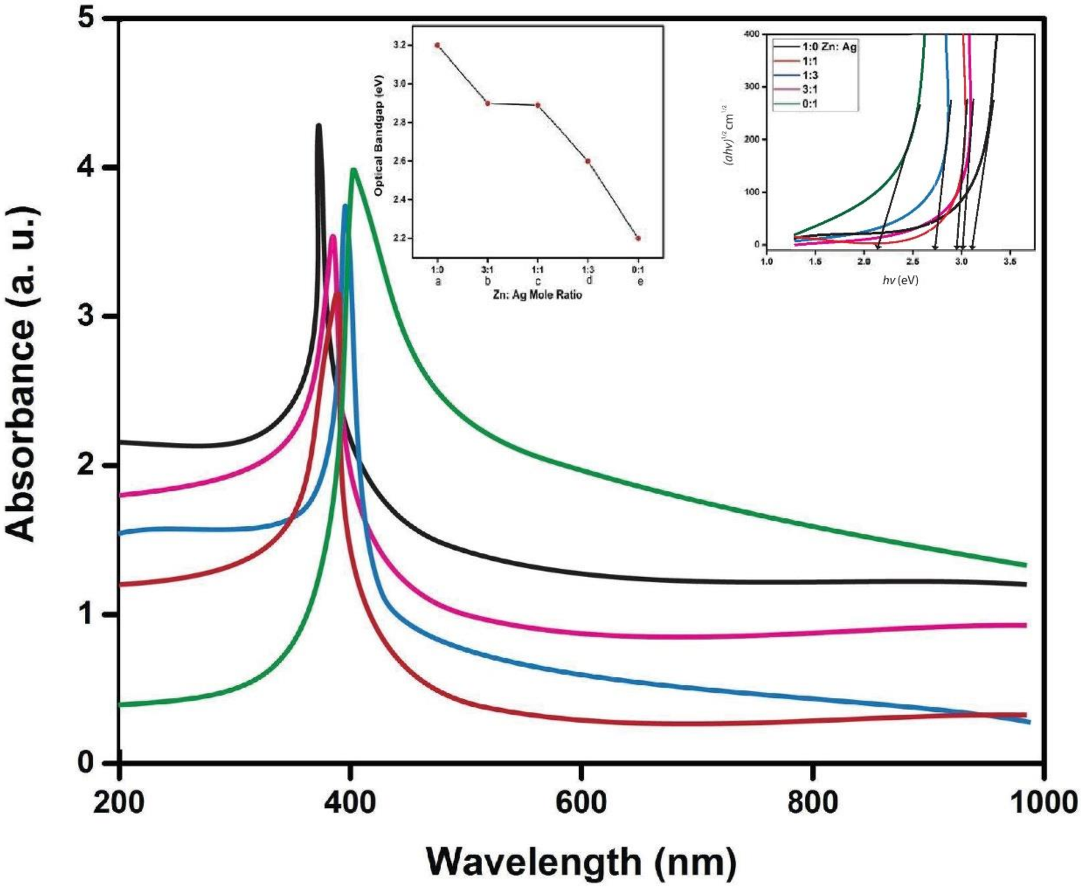

Figure 4. UV-Vis absorption spectra and Tauc plot for ZnO NR and Ag-ZnO nanostructure prepared from different molar ratio

The photocurrent density curves of pristine ZnO NRs and Ag–ZnO nanostructures prepared at various mole ratios of Zn:Ag are plotted in Figure 5. The 3:1 Zn:Ag sample had the lowest photocurrent density probably because of the high ohmic interface between the electrode and the active layer. The 0:1 Zn:Ag sample produced the highest photocurrent density can be correlated with the lowest band gap energy of 2.2 eV among all samples which has sufficiently enhanced the light absorption [25-26], in addition, the enhancement of contact between the electrode and the active layer through the hydrothermal process is also believed to have contributed in reducing the charge recombination [27]. Moreover, the abundant amounts of Ag NPs deposited onto the surface of ZnO NRs yielded an excellent visible-light absorption, leading to an efficient electron transfer and thus a high photocurrent generation. The photocurrent values presented in Table 2 were compared with the values reported by previous studies listed in Table 3. Notably, the 1:3 Zn:Ag and 0:1 Zn:Ag samples provided approximately 5-fold and 10-fold higher photocurrent densities than the pristine ZnO NR electrode, respectively. The improvement in photocurrent generation was attributed to the plasmon resonance effect of the Ag nanoparticles. Notably, the deposition of the 0:1 Zn:Ag sample produced the highest photocurrent density of 16.2 mA cm^{-2} at 1.0 V versus Ag/AgCl. Furthermore, the photocurrent generated herein was remarkably higher than that reported in previous studies [1, 28].

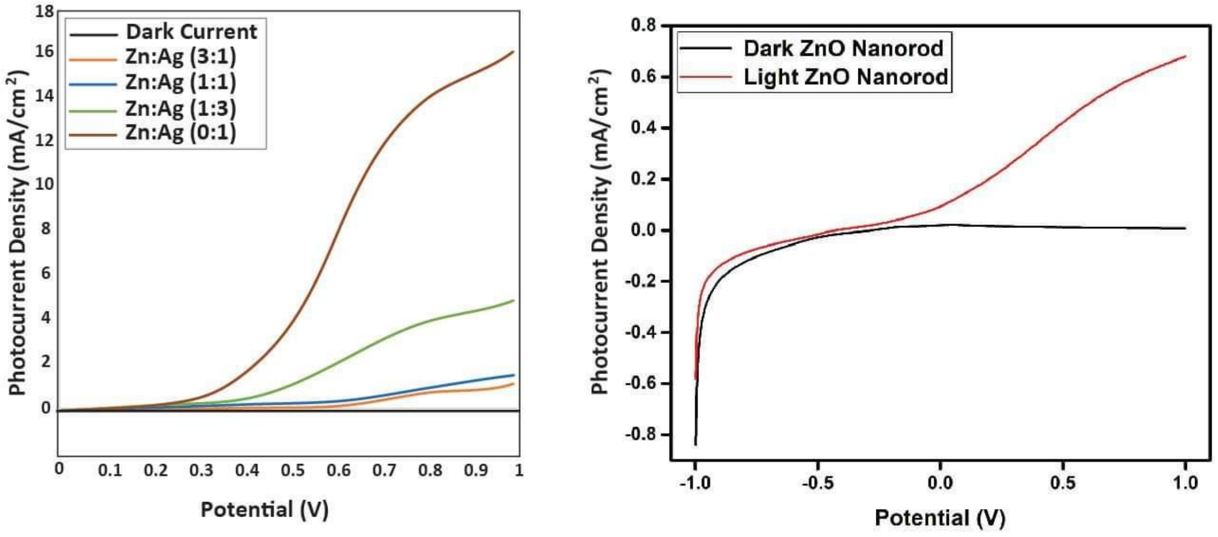

Figure 5. Photocurrent density of Zn:Ag samples synthesised at different ratios

Table 2. Photocurrent density of Zn:Ag samples synthesised at different ratios

Zn:Ag mole ratios	Photocurrent density (mA cm^{-2} at 1.0 V vs. Ag/AgCl)
1 (Zn): 0 (Ag)	0.7
3 (Zn): 1 (Ag)	1.7
1 (Zn): 1 (Ag)	2.1
1 (Zn): 3 (Ag)	4.5
0 (Zn): 1 (Ag)	16.2

Table 3. Photocurrent density of various electrodes involving Zn:Ag doping.

Synthesised Samples	**Synthesis method**	**Photocurrent density ($mA\ cm^{-2}$)**	**Voltage (V vs. Ag/AgCl)**	**Ref.**
ZnO/Ag–α-Fe_2O_3 heterostructure	Wet chemical procedures	1.40	1.0	[29]
Ag-implanted ZnO hierarchical nanoflowers	Hydrothermal route	0.08	0.4	[30]
ZnO/AgNW heterostructures	RF magnetron sputtering, polyol methods	0.46	1.0	[31]
Ag–ZnO nanostructures	RF magnetron sputtering, Hydrothermal route	16.2	1.0	Present study

4. CONCLUSION

In summary, Ag–ZnO nanostructures were prepared via a hydrothermal route. The Ag–ZnO nanostructures displayed favourable properties that make them a promising prospect as a photoanode capable of efficiently harvesting visible light. The Ag–ZnO nanostructures showed a pronounced light absorption in the visible light region. In a 0.5 M Na_2SO_4 electrolyte, the Ag–ZnO nanostructures with a molar ratio of 0:1 exhibited an excellent photocurrent density of 16.2 mA cm^{-2} at 1 V versus Ag/AgCl, which corresponded to 10-fold enhancement than that of pristine ZnO NRs under 100 mW cm^{-2} illumination. The facile, green and non-energy-intensive method presented in this study can produce highly active photoanodes. Photoactive Ag–ZnO can be used in any photocatalytic application, such as dye-sensitised solar cells, photodegradation, PEC hydrogen production and CO_2 photoreduction.

ACKNOWLEDGEMENTS

The authors gratefully acknowledge the financial support provided by the Universiti Kebangsaan Malaysia under grant numbers PKT6/2012 and DIP-2016-029. This project was also supported by Universiti Putra Malaysian under research grant number UPM-IPM-9673800.

REFERENCES

1. N. Bakranov, M. Aldabergenov, N. Ibrayev, K. Abdullin, S. Kudaibergenov, 2017 IEEE 7th International Conference Nanomaterials: Application & Properties (NAP), IEEE, 2017, pp.

03NNSA38-01-03NNSA38-04.
2. Y.-H. Nien, G.-M. Hu, M. Rangasamy, Z.-R. Yong, J.-C. Chou, C.-H. Lai, P.-Y. Kuo, J.-X. Chang, Y.-C. Lin, 67 (2020) 4983-4989.
3. P. Panchal, D.R. Paul, A. Sharma, P. Choudhary, P. Meena, S. Nehra, *J. Colloid Interface Sci*., 563 (2020) 370-380.
4. N.J. Ridha, H.B.A. Kadhim, F.K.M. Alosfur, L.H. Abood, R. Madlol, 2019, pp. 030026.
5. N.J. Ridha, F.K.M. Alosfur, H.B.A. Kadhim, L.H. Aboud, N. Al-Dahan, *J. Mater. Sci-Mater El*., 31 (2020) 9835-9845.
6. N.J. Ridha, F.K.M. Alosfur, M.H.H. Jumali, K.J. Tahir, R.A. Madlol, N. Al-Dahan, 2020, pp. 050052.
7. A. Alexandrov, M. Zvaigzne, D. Lypenko, I. Nabiev, P. Samokhvalov, *Sci. Rep*., 10 (2020) 1-11.
8. H.-M. Kim, S. Cho, J. Kim, H. Shin, J. Jang, *ACS Appl. Mater. Inter*., 10 (2018) 24028-24036.
9. R. Azmi, G. Seo, T.K. Ahn, S.-Y. Jang, *ACS Appl. Mater. Inter*., 10 (2018) 35244-35249.
10. S.S. Patil, M.G. Mali, M.S. Tamboli, D.R. Patil, M.V. Kulkarni, H. Yoon, H. Kim, S.S. Al-Deyab, S.S. Yoon, S.S. Kolekar, *Catal. Today*, 260 (2016) 126-134.
11. K.G. Stamplecoskie, J.C. Scaiano, *Photochem. Photobiol*., 88 (2012) 762-768.
12. H. Zhao, X. Zheng, X. Feng, Y. Li, *J. Phys. Chem*. C, 122 (2018) 18949-18956.
13. Y. Chen, S. Ji, W. Sun, Y. Lei, Q. Wang, A. Li, W. Chen, G. Zhou, Z. Zhang, Y. Wang, *Angew. Chem. Int. Ed.*, 59 (2020) 1295-1301.
14. H. Karimi-Maleh, B.G. Kumar, S. Rajendran, J. Qin, S. Vadivel, D. Durgalakshmi, F. Gracia, M. Soto-Moscoso, Y. Orooji, F. Karimi, *J. Mol. Liq*., 314 (2020) 113588.
15. S. Masoumi, E. Nadimi, F. Hossein-Babaei, *PCCP*, 20 (2018) 14688-14693.
16. X. Yang, L. Qiu, X. Luo, *RSC advances*, 8 (2018) 4890-4894.
17. D. Salem, M. Shalabi, F. Souissi, F. Nemmar, M.S. Belkaid, M. Aamir, J.-M. Nunzi, *EPJ Appl. Phys.*, 90 (2020) 30201.
18. H. Bian, Z. Zhang, X. Xu, Y. Gao, T. Wang, *Physica E*., 124 (2020) 114236.
19. D. Vidyasagar, S.G. Ghugal, A. Kulkarni, P. Mishra, A.G. Shende, S.S. Umare, R. Sasikala, *Appl. Catal. B-Environ.*, 221 (2018) 339-348.
20. M. Ajili, M. Castagné, N.K. Turki, 53 (2013) 213-222.
21. H. He, J. Fei, J. Lu, *J. Nanostructure Chem*., 5 (2015) 169-175.
22. N.A. Albadarin, M.S. Takriff, S.T. Tan, S.A. Shahahmadi, L.J. Minggu, A.A.H. Kadhum, W.W. Yin, M.N.I. Salehmin, E.M. Alkhalqi, M.A.A. Hamid, *Mater. Res. Express*, 7 (2020) 125010.
23. S. Khosravi-Gandomani, R. Yousefi, F. Jamali-Sheini, N.M. Huang, *Ceram. Int*., 40 (2014) 7957-7963.
24. A. Ievtushenko, V. Karpyna, J. Eriksson, I. Tsiaoussis, I. Shtepliuk, G. Lashkarev, R. Yakimova, V. Khranovskyy, *Superlattice Microst*., 117 (2018) 121-131.
25. A. Hemmani, A. Nouri, H. Khachab, T. Atouani, *Int. J. Renewable Energy Research,* 7 (2017) 525-530.
26. M.N.I. Salehmin, L.J. Minggu, W.F. Mark-Lee, M.A. Mohamed, K. Arifin, M.H.H. Jumali, M.B. Kassim, *Sol. Energy Mater. Sol. Cells*, 182 (2018) 237-245.
27. T. Gupta, J. Cho, J. Prakash, *Mater. Today Chem*., 20 (2021) 100428.
28. B.J. Rani, A. Anusiya, M. Praveenkumar, S. Ravichandran, R.K. Guduru, G. Ravi, R. Yuvakkumar, *J. Mater. Sci-Mater El*., 30 (2019) 731-745.
29. G. Kaur, S.A. Khan, V.R. Satsangi, S. Dass, R. Shrivastav, *Renew. Energ*., 164 (2021) 156-170.
30. A. Sreedhar, I.N. Reddy, Q.T.H. Ta, G. Namgung, J.-S. Noh, *J. Electroanal. Chem*., 832 (2019) 426-435.
31. J. Han, Z. Liu, K. Guo, X. Zhang, T. Hong, B. Wang, *Appl. Catal. B-Environ*., 179 (2015) 61-68.